

Accurate Screening of Functional Materials with Machine-Learning Potential and Transfer-Learned Regressions: Heusler Alloy Benchmark

Enda Xiao^{1*} and Terumasa Tadano^{1,2*}

¹Research Center for Magnetic and Spintronic Materials, National Institute for Materials Science, 1-2-1 Sengen, Tsukuba, 305-0047, Ibaraki, Japan.

²Digital Transformation Initiative Center for Magnetic Materials (DXMag), National Institute for Materials Science, 1-2-1 Sengen, Tsukuba, 305-0047, Ibaraki, Japan.

*Corresponding author(s). E-mail(s): Xiao.Enda@nims.go.jp;
Tadano.Terumasa@nims.go.jp;

Abstract

A machine learning-accelerated high-throughput (HTP) workflow for the discovery of magnetic materials is presented. As a test case, we screened quaternary and all-*d* Heusler compounds for stable compounds with large magnetocrystalline anisotropy energy (E_{aniso}). Structure optimization and evaluation of formation energy and distance to hull convex were performed using the eSEN-30M-OAM interatomic potential, while local magnetic moments, phonon stability, magnetic stability, and E_{aniso} were predicted by eSEM models trained on our DxMag Heusler database. A frozen transfer learning strategy was employed to improve accuracy. Candidate compounds identified by the ML-HTP workflow were validated with density functional theory, confirming high predictive precision. We also benchmark the performance of different MLIPs, and discuss the fidelity of local magnetic moment prediction and its extension to other magnetic materials.

1 Introduction

The [high-throughput \(HTP\)](#) screening approach has emerged as a powerful strategy for accelerating the discovery of novel materials by systematically exploring large chemical spaces computationally or experimentally [1–3]. The [density functional theory \(DFT\)](#) based [HTP](#) workflows have been widely employed to identify materials with target properties. However, as the search space increases, the associated computational cost becomes unsustainable, often restricting screening efforts to a manageable subspace [4, 5]. To address this bottleneck, [machine learning \(ML\)](#) offers a promising route by drastically reducing computational costs. In this work, we demonstrate the robust integration of state-of-the-art [ML](#) techniques into the [HTP](#) workflow (ML-HTP) through a practical case study focused on screening quaternary and all-*d* Heusler compounds for stable candidates with strong [magnetic anisotropy energy \(\$E_{\text{aniso}}\$ \)](#).

Initial realizations of the ML-HTP paradigm relied on [ML](#) models that utilize compositional descriptors as input embeddings [6–8]. These models directly map chemical formulas to target properties, offering efficiency and simplicity. However, composition-based models are inherently unable to distinguish compounds with identical stoichiometry but different atomic arrangements. One workaround involves assigning layer indices to atomic sites, but this approach fixes the number of sites and can yield inconsistent predictions for symmetry-equivalent structures [9, 10]. Crystal graph based models do not have such drawbacks since they explicitly incorporate structure information as input, capturing structure-property relationships more accurately [11, 12]. However, crystal graph based models introduce an additional computational step, as geometry optimization must precede property prediction.

Although a single [DFT](#) optimization typically requires only a few minutes, the cumulative cost of screening a large number of candidate compounds becomes prohibitively expensive, particularly for magnetic systems where multiple magnetic configurations must be considered. A promising solution lies in leveraging [machine](#)

learning interatomic potentials (MLIPs), which can accelerate structure optimization by several orders of magnitude relative to DFT. The MLIP field has witnessed rapid advancements in recent years, with many crystal graph based models proposed. Despite the conceptual appeal, reliable and robust MLIP-based structure optimization has only become practical recently, especially following the release of the large-scale and diverse Meta Open Materials 2024 Dataset (OMat24) training dataset in 2024 [13]. This is demonstrated in the current work by benchmarking several MLIPs, ranging from early-stage implementations to state-of-the-art developments.

With optimized structures, property can be predicted using machine learning regressor model (MLRM). This approach substantially reduces computational cost, particularly for properties that are expensive to compute via DFT, such as phonon spectra, conductivity, magnetic critical temperature (T_c), and E_{aniso} . However, training accurate MLRMs typically requires large, high-quality datasets. To overcome this challenge, transfer learning (TL) techniques can be employed to adapt pretrained ML models to new tasks [14–16]. TL leverages models that have already learned generalizable representations from extensive datasets and fine-tunes them using smaller, task-specific datasets. This strategy enhances predictive accuracy while substantially reducing data requirements.

As a case study, we conducted a ML-HTP screening focused on Heusler compounds, which have garnered significant attention due to their diverse functional properties, technological potential, and the structure complexity [17]. Numerous DFT-HTP screenings have been carried out to identify candidates with different desirable properties [1, 4, 5, 18–20]. In our previous work, we developed DXMag Computational Heusler Database (HeuslerDB), a comprehensive database encompassing nearly all conventional ternary Heusler compounds. The present study significantly extended the search space to include quaternary and all- d Heusler compounds, targeting stability and E_{aniso} as key screening criteria. In earlier DFT-HTP studies, 10 large E_{aniso}

candidates were identified out of 286 selected compositions, and 15 among 29,784 Co-based structures [4, 5]. This low yield underscores the rarity of such materials and highlights the difficulty of this search problem, making it a stringent test case for ML-HTP approaches.

In this work, we demonstrate the use of MLIP and TL-MLRMs as drop-in replacements for DFT structure optimization and property evaluation within HTP framework, as illustrated in Fig. 1(a). As a practical application, we employed this approach to identify conventional quaternary and all-*d* Heusler compounds with large E_{aniso} , while simultaneously satisfying thermodynamic, dynamic, and magnetic stability. Structure optimization and thermodynamic stability evaluation were performed using the eSEN-30M-OAM MLIP. The following predictions of local magnetic moment ($\{\mathbf{m}_i\}$), minimum phonon frequency (ω_{min}), T_c , and E_{aniso} were performed using MLRMs. The MLRMs were trained via frozen transfer learning, using eSEN-30M-OAM MLIP as the base model and fine-tuned using HeuslerDB data and newly computed data. Identified candidates were validated through DFT calculations to demonstrate the significant reliability of this ML-HTP approach. We further examine key factors that influence the performance of such ML-HTP workflows, including accuracy of MLIP-based structure optimization, the magnetic configuration prediction, and the frozen transfer learning technique.

2 Results

To accumulate data for training E_{aniso} MLRM, we first computed the E_{aniso} of conventional ternary Heusler compounds within HeuslerDB using DFT. The E_{aniso} of some Heusler compounds were reported in the previous work and the agreement between our DFT results and previous work is demonstrated in the Supplementary Materials [4, 5]. Among all conventional ternary Heusler compounds, 2190 (7.9 %) exhibit E_{aniso} magnitude greater than 1 MJ/m³. When further screened for thermodynamic,

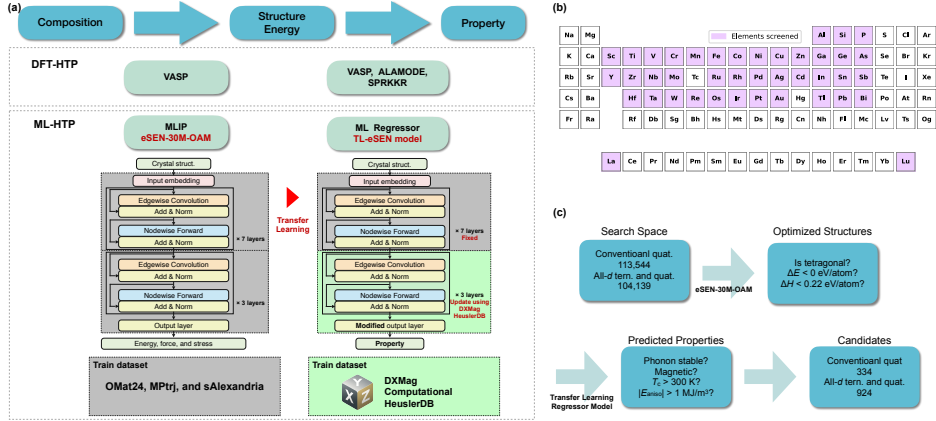


Fig. 1 (a) Workflow overview of **MLIP** and **TL-MLRM** as a drop-in replacement for DFT in **HTP** screening. The **TL-MLRM** is initialized from the **eSEN-30M-OAM MLIP**, with the embedding layers and the first seven layers held fixed during training. The eSEN architecture schematic is adapted from the original publication introducing the model [21]. (b) Compositional space covered in the **HTP** screening. (c) Detailed **HTP** workflow for identifying conventional quaternary and all-*d* Heusler compounds with stability and strong E_{aniso} .

dynamical, and magnetic stability, only 135 compounds (0.5 %) meet both the high E_{aniso} and stability criteria. These low percentages underscore the difficulty of identifying stable, high E_{aniso} compounds and highlight the need for more efficient screening methods demonstrated in current work. The compositional space covered in ML-HTP is shown in Fig. 1(b) and the ML-HTP workflow containing selection criteria is shown in Fig. 1(c). The detailed workflow and computation methods are described in Sec. 4.

2.1 Validation of ML-HTP selected candidates

Using **eSEN-30M-OAM MLIP** in combination with **MLRMs**, we screened almost all conventional quaternary and all-*d* ternary and quaternary Heusler spaces for stable compounds with high E_{aniso} . Among 131,544 conventional quaternary Heusler and 104,139 all-*d* Heusler compounds, the workflow yielded 366 and 924 candidates, respectively. To evaluate the reliability of this ML workflow, all candidates were validated using DFT calculations and the results are provided in the Supplementary Materials. The validation results are summarized in Fig. 2 as *ML-HTP quat.* and *ML-HTP all-d* bins and the performances across *c/a* ratio, formation energy (ΔE), distance to convex

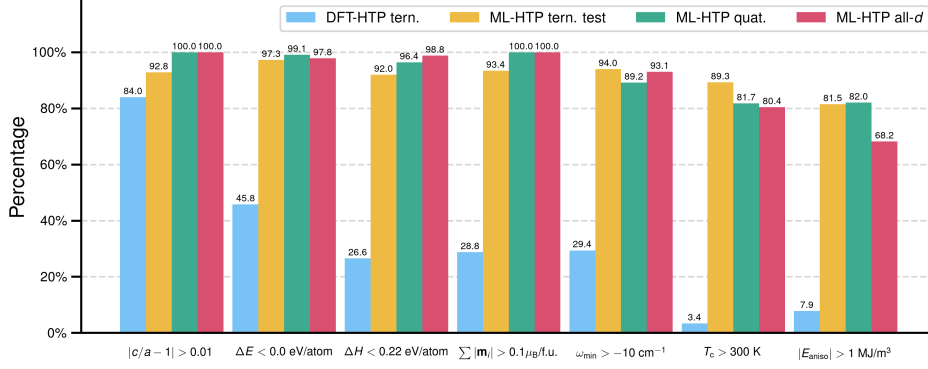


Fig. 2 Validation summary of ML-HTP approach. For candidate lists of conventional quaternary and all-*d* Heusler compounds, the percentages that satisfy the screening criteria by DFT validation are shown (*ML-HTP quat.* and *ML-HTP all-d*). The precision of the ML models, as measured on the test set of conventional ternary compounds, is also reported (*ML-HTP tern. test*). To demonstrate efficiency improvement, the percentages of compounds in the whole conventional ternary Heusler space that meet the same criteria using DFT-HTP screening are included (*DFT-HTP tern.*).

$\text{hull}(\Delta H)$, $\{\mathbf{m}_i\}$, ω_{\min} , T_c , and E_{aniso} are shown. For each property, the percentage of candidates meeting the screening criterion in DFT validation is reported. The precisions of the ML models, measured on the test set of conventional ternary compounds, are also provided as *ML-HTP tern. test* bins for comparison. To demonstrate the efficiency improvement, the percentages of compounds in the all conventional ternary Heusler space that satisfy the same criterion are included and marked as *DFT-HTP tern.*

In ML-HTP, the c/a ratio, ΔE , and ΔH are obtained from optimized structure and the corresponding energy by **eSEN-30M-OAM MLIP**. Since a non-zero E_{aniso} requires the Heusler compound to adopt a tetragonal phase, we applied a screening threshold of $|c/a - 1| > 0.01$ to identify tetragonality. Notably, all ML-selected candidates remained tetragonal in DFT validation, confirming that **eSEN-30M-OAM** reliably distinguishes between cubic and tetragonal phases. A more detailed discussion of the prediction performance for lattice parameters a , c , and the c/a ratio, and comparisons with other **MLIP** models, are provided in Sec. 2.3.

Using energies of candidate compounds, elements, and competing phases predicted by eSEN-30M-OAM, the ΔE and ΔH were calculated. The criteria of $\Delta E < 0$ eV/atom and $\Delta H < 0.22$ eV/atom were employed to identify thermodynamically stable candidates, following the thresholds established in our previous DFT-HTP study [20]. Among ML-selected candidates, 99.1% of conventional quaternary and 97.8% of all-*d* Heusler compounds were validated to have $\Delta E_{\text{DFT}} < 0$ eV/atom. Similarly, 96.4% (quaternary) and 98.8% (all-*d*) of the compounds were found to have $\Delta H_{\text{DFT}} < 0.22$ eV/atom. These high validation rates demonstrate that state-of-the-art MLIPs, such as eSEN-30M-OAM, can reliably assess thermodynamic stability.

It is important to note that the eSEN-30M-OAM MLIP used is a general-purpose, pretrained model without any fine-tuning specific to the Heusler chemical space. Thus, these results highlight its strong generalization, making it an effective drop-in replacement for DFT-based optimization and thermodynamic stability assessment in HTP workflow. Notably, the model achieves strong performance on the studied magnetic systems, despite not explicitly incorporating magnetic moments into its architecture or training. This strong performance and generalization is particularly valuable for the initial screening of novel material systems, where MLIPs can greatly reduce the search space by rapidly and reliably estimating optimized structures and thermodynamic stability.

The properties $\{\mathbf{m}_i\}$, ω_{min} , T_c , and E_{aniso} were predicted using MLRMs applied to MLIP-optimized structures. Because E_{aniso} is a magnetic property, $\{\mathbf{m}_i\}$ was first predicted, and a screening threshold of $\sum |\mathbf{m}_i| > 0.1 \mu_{\text{B}}/\text{f.u}$ was applied to identify magnetic compounds. DFT validations confirmed that this classification achieved 100% precision. Moreover, the $\{\mathbf{m}_i\}$ MLRM accurately predicts both the magnitude and sign of local moments, as discussed in detail in Sec. 2.5. Magnetic system identification is a critical yet computationally demanding step in DFT-HTP, as multiple initial $\{\mathbf{m}_i\}$ values must be tested and the low fraction of magnetic systems in some

material families can lead to substantial wasted computation. By incorporating the $\{\mathbf{m}_i\}$ MLRM method as a pre-screening step, the search space can be substantially reduced.

To identify compounds with dynamic stability, magnetic stability, and large E_{aniso} , we applied the criteria $\omega_{\text{min}} > -10 \text{ cm}^{-1}$, $T_c > 300 \text{ K}$, and $|E_{\text{aniso}}| > 1 \text{ MJ/m}^3$. Among the ML-selected candidates, 89.2% of conventional quaternary and 93.1% of all- d Heusler compounds were validated to have ω_{min} above -10 cm^{-1} . For magnetic stability, 81.7% of conventional quaternary and 80.4% of all- d Heusler compounds were validated to have T_c above 300 K. For the target property E_{aniso} , the validation rates were 82.0% and 68.2%, respectively. In contrast, our DFT-HTP survey of all conventional ternary compounds finds that only 3.4% have $T_c > 300 \text{ K}$ and 7.9% have $E_{\text{aniso}} > 1 \text{ MJ/m}^3$. The high precision of the ML approach yields substantial efficiency gains compared with conventional DFT-HTP screening across the full chemical space.

The MLRMs were trained exclusively using train set of conventional ternary Heusler compounds, yet were applied to evaluate quaternary and all- d compositions. By comparing validation rates to the precisions calculated using the test set of conventional ternary compounds, the MLRMs for $\{\mathbf{m}_i\}$ and T_c generalize well to these expanded chemical spaces. In contrast, the E_{aniso} model exhibits lower performance for all- d compounds. This discrepancy can be attributed to the difference in chemical environments: while conventional quaternary compounds retain Z -site elements from the p -block—consistent with the training set—all- d compounds introduce Z elements from the d -block, which were absent during training. E_{aniso} is a sensitive property, influenced by subtle details of the electronic structure, and thus more susceptible to domain shifts than $\{\mathbf{m}_i\}$ or T_c .

Relaxing the screening thresholds increases the pool of candidate compounds and captures promising cases missed initially, though at the expense of reduced precision. Nonetheless, the curated list of compounds that meet stability criteria, and further

magnetic system criterion, serves as an efficient starting point for investigation of additional functional properties. For readers interested in exploring an expanded candidate list, the full set of ML-HTP predicted data of 113,544 conventional quaternary and 104,139 all-*d* Heusler compounds will be added to the [HeuslerDB](https://www.nims.go.jp/group/spintheory/), which is publicly available at <https://www.nims.go.jp/group/spintheory/>.

2.2 Distribution of strong E_{aniso} candidates

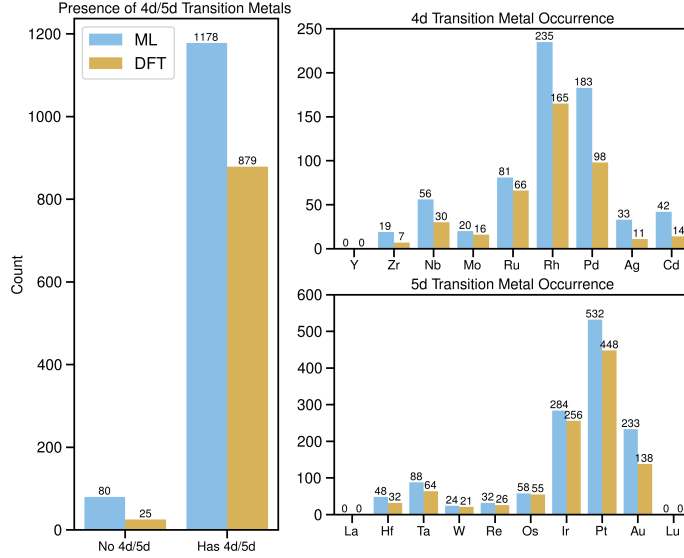


Fig. 3 Distribution of ML-selected candidate compounds based on whether 4d or 5d elements are present and distribution over 4d and 5d elements contained. The distribution of DFT validated strong E_{aniso} candidates is also shown.

In addition to validating predictive precision, it is essential to determine whether the ML models capture known physical trends. A well-established insight is that compounds containing 4*d* and 5*d* elements typically exhibit larger E_{aniso} than those composed of 3*d* elements, owing to the stronger spin-orbit coupling associated with the heavier atomic nuclei of 4*d* and 5*d* elements. This behavior is clearly reproduced in the ML-HTP results, as shown in Fig. 3, which presents the distribution of candidate compounds according to the presence of 4*d*/5*d* elements. The figure further

highlights the specific $4d/5d$ elements that appear in the identified compounds. For comparison, Fig.3 also includes the distribution of compounds with DFT-calculated E_{aniso} magnitudes exceeding 1 MJ/m³.

2.3 MLIPs optimization performance

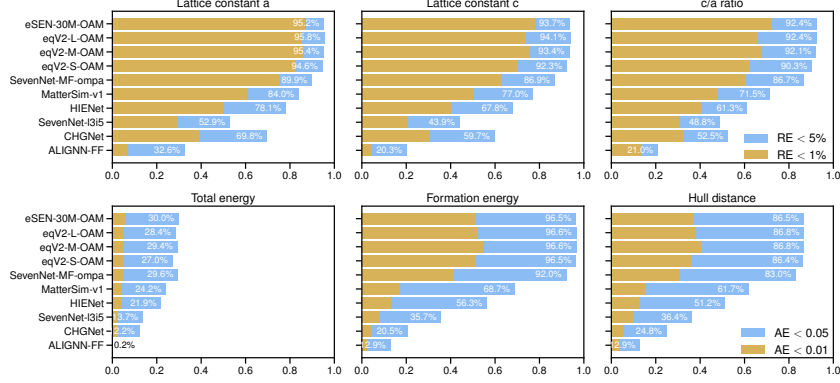


Fig. 4 Lattice constants a and c , c/a ratio, total energy (E), formation energy (ΔE), and convex hull distance (ΔH) predicted by various MLIPs are benchmarked against DFT references. For each property, the fraction of compounds with predictions falling within specified relative error (RE) or absolute error (AE) thresholds is reported. Energetic quantities (E , ΔE , and ΔH) are expressed in eV/atom.

In recent years, MLIPs have advanced rapidly, with numerous new models proposed and trained. To identify the most suitable model for our screening workflow, we benchmarked representative MLIPs models developed since 2023. These include ALIGNN-FF, CHGNet, SevenNet-l3i5, SevenNet-MF-ompa, HIENet, MatterSim-v1, eqV2-S-OAM, eqV2-M-OAM, eqV2-L-OAM, and the latest eSEN-30M-OAM [13, 21–26]. The evaluation focused on structure optimization for 10,000 conventional ternary compounds randomly selected from the ground states in HeuslerDB. To identify global minimum, 14 initial structures were generated by applying strain to the conventional cell (two formula units) and converting it to the primitive cell (one formula unit). Specifically, the a , b , and c axes were uniformly scaled by $\pm 10\%$ and $\pm 30\%$, or the c -axis alone was varied by $\pm 10\%$, $\pm 20\%$, $\pm 30\%$, $\pm 40\%$, and $\pm 50\%$.

The performance of structure optimization was assessed by comparing the predicted lattice constants a and c , and the resulting c/a ratio, with corresponding DFT values. The results are summarized in Fig. 4. The relative error (RE) is defined as the maximum of $\left| \frac{x_{\text{ML}}}{x_{\text{DFT}}} - 1 \right|$ and $\left| \frac{x_{\text{DFT}}}{x_{\text{ML}}} - 1 \right|$, where x_{ML} and x_{DFT} denote the values predicted by the ML and DFT, respectively. We report the fractions of compounds within 5% and 1% RE tolerances. Among the evaluated models, the eSEN-30M-OAM and eqV2 models achieved the highest accuracy at 5% RE, with eSEN-30M-OAM showing slightly better performance at the stricter 1% RE threshold. A key distinction between the two models lies in the number of local minima encountered: eqV2-L-OAM (91,585) produced substantially more than eSEN-30M-OAM (32,606). This difference arises from the smoother energy landscape of eSEN-30M-OAM, enabling fewer initial structures to converge to the global minimum and thereby improving optimization efficiency. Convergence tests of all evaluated models are provided in the Supplementary Materials.

The predictive performance of total energy (E), formation energy (ΔE), and energy above the convex hull (ΔH) using MLIP was assessed by comparing the MLIP predictions with DFT values, using the absolute error (AE), $|x_{\text{ML}} - x_{\text{DFT}}|$. The fractions of compounds with AE below 0.01 and 0.05 eV/atom are shown in Fig. 4. Among the benchmarked models, eSEN-30M-OAM and the eqV2 variants showed the highest accuracy for ΔE and ΔH at the 0.05 eV/atom threshold, with eSEN-30M-OAM displaying a slight drop in accuracy at the more stringent 0.01 eV/atom level. Predicted total energies from MLIP were found to be systematically lower than DFT values, reducing direct agreement; however, this offset also applies to elemental references and competing phases, so the relative quantities ΔE and ΔH remain in strong agreement with DFT. Given its robust performance in both structure optimization and thermodynamic stability, eSEN-30M-OAM was selected for integration into the ML-HTP workflow.

Previous studies have reported the performance of composition-based models in predicting lattice constants, ΔE , and ΔH for cubic Heusler compounds. For comparison, we evaluated metric of eSEN-30M-OAM on the cubic Heusler subset, with results summarized in Table 1. The R^2 score for the lattice constant a is 0.994, surpassing the previously reported ranges of 0.80–0.94 across different Heusler types and the values of 0.94, 0.979, and 0.987 in other works [8, 10, 27, 28]. Similarly, the R^2 for ΔE reaches 0.995, outperforming earlier results of 0.80–0.88 and 0.93, 0.982 [8, 10, 27]. The R^2 for ΔH is 0.98, exceeding prior values of 0.91 and 0.969 [10, 29]. The root mean squared errors (RMSE) for a and ΔE are 0.02 Å and 0.029eV/atom, respectively, which are significantly lower than the 0.11Å and 0.117eV/atom reported in earlier work[9].

Table 1 Performance comparison of the eSEN MLIP and MLRM with ALIGNN models and previously reported results. The size of dataset used for MLRM is also listed.

Property	Metric	eSEN-30M-OAM	ALIGNN-FF	Previous reports	
a	R^2	0.994	0.128	0.80–0.94 ¹ , 0.94 ² , 0.987 ³ , 0.979 ⁴	
	RMSE	0.023	0.330	0.110 ⁵	
ΔE	R^2	0.995	0.453	0.80–0.88 ¹ , 0.93 ² , 0.982 ³	
	RMSE	0.029	0.310	0.117 ⁵	
ΔH	R^2	0.980	0.330	0.91 ⁶ , 0.969 ³	
Property	Metric	eSEN MLRM	ALIGNN MLRM	Previous reports	Dataset size
$\{m_i\}$	R^2	0.990		—	27,864
m_{total}	R^2	0.986	0.90	0.75–0.89 ¹ , 0.82 ⁷ , 0.90 ³	27,864
$\sum m_i $	R^2	0.990	0.89	—	27,864
ω_{min}	R^2	0.750	0.73	—	8,198
T_c	R^2	0.910	0.84	0.76 ⁸ , 0.73 ⁹	2,106
	Accu.	0.910		0.73 ⁸	
E_{aniso}	R^2	0.680	0.59	—	6,123

¹[8] Dataset size is about 1000, ²[27] Dataset size is about 65,000,

³[10] Dataset size is about 500,000 for a and m_{total} , and about 450,000 for ΔE and ΔH ,

⁴[28] Dataset size is 143, ⁵[9] Dataset size is 16,272, ⁶[29] Dataset size is 426,148,

⁷[30] Dataset size is 1153, ⁸[6] Dataset size is 408, ⁹[31] Dataset size is 6500.

2.4 Improvements Over Existing Approaches

The MLRMs used in screening were trained on the data from HeuslerDB, supplemented with newly computed T_c and E_{aniso} values using optimized structures in HeuslerDB. Test set metrics are summarized in Table 1 and benchmarked against previously reported results. The MLRM for $\{\mathbf{m}_i\}$ achieved an R^2 score of 0.990. For comparison with prior studies that used total magnetization (m_{total}) as the target property, our model yielded $R^2 = 0.986$ for m_{total} , exceeding earlier values of 0.75–0.89, 0.82, and 0.90 [8, 10, 30]. For T_c , the model attained $R^2 = 0.91$ and classification accuracy of 0.91, both substantially higher than previously reported values of $R^2 = 0.76$ and 0.73 and accuracy of 0.73 [6, 31].

To the best of our knowledge, no previous study has predicted phonon stability or E_{aniso} of Heusler compounds using ML. The effectiveness of the ω_{min} and E_{aniso} models developed here is supported by the validation results in Sec. 2. While phonon stability could also be assessed using MLIP combined with conventional phonon calculation methods, a detailed comparison between this MLIP-based strategy and the MLRM approach adopted in our workflow is left for future work focused on phonon properties and their interactions. The E_{aniso} model achieved an R^2 of 0.68—lower than those of $\{\mathbf{m}_i\}$, ω_{min} , and T_c —highlighting the higher sensitivity and complexity of E_{aniso} as a target property. Nevertheless, despite the reduced R^2 , its classification accuracy remains satisfactory and sufficient for integration into the ML-HTP workflow.

To benchmark advances in ML techniques since 2023, we applied the ALIGNN-FF MLIP and ALIGNN MLRM to identify conventional quaternary candidate compounds and evaluated the validation rates of strong E_{aniso} compounds [12, 22]. In this test, the scalar quantity $\sum |\mathbf{m}_i|$ was used directly as the target property rather than being calculated from $\{\mathbf{m}_i\}$ prediction. The metrics of ALIGNN-FF and ALIGNN MLRM are summarized in Table 1. Using all screening thresholds, only 17 compounds qualified as candidates. To improve statistical robustness, we removed the

phonon stability criterion, expanding the candidate list to 107 compounds, of which 26 (25.2%) exhibit $|E_{\text{aniso}}| > 1\text{MJ/m}^3$. While this yield is notably higher than the 7.9% obtained from direct DFT-HTP screening, it remains far below the 82.0% success rate achieved with the eSEN-based ML-HTP workflow. These results highlight the substantial improvements in screening precision enabled by the state-of-the-art eSEN model.

We further tested a hybrid workflow in which structure optimization was performed with eSEN-30M-OAM MLIP, while property prediction was carried out using ALIGNN MLRMs. This approach yielded 276 candidate compounds, of which 149 (54.0%) were confirmed by DFT to exhibit strong E_{aniso} . The improved yield relative to ALIGNN-FF based optimization underscores the critical importance of accurate structure optimization with eSEN-30M-OAM for enhancing ML-HTP screening. However, the yield still falls short of the 82.0% achieved by the fully eSEN-based workflow, indicating that progress in both the MLIP and MLRM components is essential for maximal efficiency. We also tested the inverse hybrid configuration, using ALIGNN-FF MLIP for structure optimization combined with eSEN MLRMs for property prediction. This workflow identified 243 candidates, of which only 76 (31.3%) were validated as strong E_{aniso} compounds. This marked reduction in performance highlights the pivotal role of selecting an accurate MLIP for structure optimization.

2.5 Prediction of local magnetic moment

Since the goal of this study is to identify compounds with large E_{aniso} , it is first necessary to determine whether a compound is magnetic. Relying solely on the total magnetization is inadequate, as it cannot capture antiferromagnetic (AFM) or low-moment ferrimagnetic (FiM) compounds. To address this, we employed the total absolute magnetic moment, defined as $\sum_i |\mathbf{m}_i|$, where \mathbf{m}_i denotes the local magnetic moment at atomic site i .

Local magnetic moments were predicted using an [MLRM](#) based on the eSEN architecture, trained to output the moment at each atomic site. Restricting to collinear configurations that all moments aligned along the z -axis, each moment is represented by a scalar whose sign encodes the direction, with $\ell = 0$ per site in the output head. To account for the z -direction ambiguity—where a configuration and its sign-inverted counterpart (i.e., all local moments flipped) are physically equivalent—we modified the loss function to compute losses for both the predicted $\{\mathbf{m}_i\}$ and its sign-inverted counterpart, and use the smaller value as the loss. This ensures invariance under global spin inversion.

Fig 5 (a) shows a scatter plot comparing $\{\mathbf{m}_i\}$ from the [MLRM](#) and [DFT](#) for compounds in test set, with histograms along the axes illustrating their distributions. Local moments at the atom site Z are omitted as they are non-magnetic. Because 73.4% of the test compounds are non-magnetic, both histograms exhibit a pronounced peak at zero. For magnetic systems, the global sign is adjusted so that the total magnetic moment is positive; since most magnetic compounds are ferromagnetic, positive moments dominate in the distribution. Nearly all points fall along the diagonal, demonstrating that the model accurately reproduces both the magnitude and sign of local moments, and reliably distinguishes ferromagnetic (FM) and ferrimagnetic (FiM) systems. Only 1.4% of points lie along either axis, corresponding to DFT-magnetic sites incorrectly predicted as non-magnetic or vice versa, indicating highly accurate magnetic/non-magnetic classification.

Predicting $\{\mathbf{m}_i\}$ is a common yet computationally demanding step in [HTP](#) studies of magnetic materials. The approach developed in this work achieves high accuracy in $\{\mathbf{m}_i\}$ prediction and is readily transferable to other systems. A central question, however, is how many training compounds are required to reach satisfactory accuracy. To address this, we performed a learning-curve analysis by training the [MLRM](#) on progressively larger subsets of the dataset and evaluating performance on a fixed

validation set of 5000 compounds, of which 1486 are magnetic. For evaluation, local moments at the X_1 , X_2 , and Y sites were concatenated across samples into a single array, while the Z site was excluded since it is non-magnetic in conventional Heusler compounds.

The learning curve is shown in Fig. 5 (b), illustrating how model performance improves with increasing training set size. In the top panel, the R^2 scores for both local moments and their magnitudes are presented. The gap between the two curves indicates that, while the model generally captures the magnitude accurately, it sometimes assigns the incorrect sign. For example, Mn_2ScGe with DFT-computed local moments $\{2.62, 3.03, -0.29, -0.10\} \mu_B$ is predicted as $\{-2.71, 3.04, 0.02, -0.02\} \mu_B$ by **MLRM**. The bottom panel reports two key metrics: (i) classification accuracy for identifying magnetic systems and (ii) the fraction of local moments with absolute error below $0.1 \mu_B$, evaluated across all compounds and within the magnetic subset. With 5000 training samples, the model achieves a classification accuracy of 0.92, and 90% of all compounds fall within the $0.1 \mu_B$ error threshold. However, this fraction decreases to 0.72 when restricted to magnetic compounds, indicating that the model identifies whether a site is magnetic with high reliability but remains less accurate in predicting exact $\{\mathbf{m}_i\}$ values. Increasing the training set to 125,000 samples improves this fraction to 0.82, while relaxing the threshold to $0.2 \mu_B$ further raises it to 0.92. Although performance improves with larger datasets, the gains become progressively smaller. These results highlight the critical role of dataset size in improving $\{\mathbf{m}_i\}$ accuracy and inform the selection of training size in future work focusing on other magnetic systems.

2.6 Frozen transfer learning for **MLRM** construction

To improve the performance of the **MLRM**, we employed a frozen transfer learning strategy using the **eSEN-30M-OAM MLIP** as the base model. The **eSEN-30M-OAM**

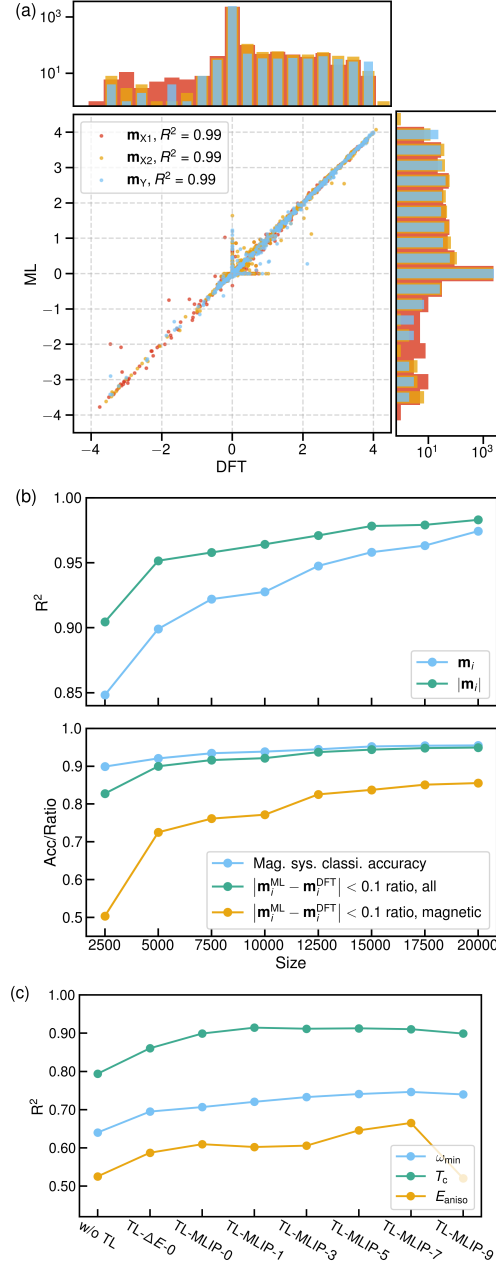


Fig. 5 (a) Scatter plot comparing ML-predicted $\{m_i\}$ with DFT values for the test set. (b) Learning curves for $\{m_i\}$ prediction. The top panel shows R^2 scores for both local moments and their magnitudes. The bottom panel reports the fraction of compounds with absolute prediction error below $0.1 \mu_B$ for all compounds and for the magnetic subset, together with magnetic system classification accuracy. (c) R^2 of models initialized from the eSEN-30M-OAM MLIP and trained with different numbers of frozen layers (denoted TL-MLIP- n). In the $n = 0$ case, the embedding layer is also trainable. A model trained from scratch (denoted w/o TL) and a transfer learning variant initialized from a base model pre-trained on ΔE data from the HeuslerDB database (denoted TL- ΔE -0) are included for comparison.

MLIP was trained on the OMat, MPtrj, and sAlexandria databases, providing a comprehensive training set spanning the periodic table [13, 23, 32–34]. Through this training, the embedding and the first several layers learn general chemical and structure representations. To leverage this, we transferred the parameters of the embedding and the first several layers into our MLRM and kept them fixed (frozen layers), while only updating the remaining layers and the output layer (flexible layers). This approach is analogous to a recent work in which the initial layers of ORB, EqV2, or MACE MLIPs were used to generate feature vectors that were subsequently passed to property prediction models such as MODNet, XGBoost, and MLP [35].

The eSEN-30M-OAM model consists of 10 layers. Figure 5 shows the R^2 scores of models trained with different numbers of frozen layers, denoted TL-MLIP- n . In the $n = 0$ case, the embedding layer is also flexible. Results for ω_{\min} , T_c , and E_{aniso} are presented. Model performance improves as the number of frozen layers increases up to $n = 7$, after which it declines when more layers are frozen. This trend reflects the balance between transferring knowledge from the base model and maintaining sufficient flexibility to adapt to the new task. Based on this analysis, TL-MLIP-7 was selected as the final model for ω_{\min} , T_c , E_{aniso} , and $\{\mathbf{m}_i\}$ MLRM. For comparison, a model trained from scratch (w/o TL) is included, which yields lower R^2 scores and highlights the benefit of transfer learning. We also tested a variant initialized from a base model pre-trained on formation energy (ΔE) data from the HeuslerDB database (denoted TL- ΔE -0). TL-MLIP-0 outperforms TL- ΔE -0, indicating that initialization from the eSEN-30m-oam model, trained on a comprehensive dataset, is more advantageous.

3 Discussion

We demonstrated the feasibility of combining MLIPs and MLRMs for HTP screening. As a case study, we identified 334 conventional quaternary Heusler compounds and 924 all- d Heusler compounds that exhibit thermodynamic, dynamical, and magnetic

stability, together with large E_{aniso} . The precision of this workflow was confirmed through DFT validation of the candidate list.

When a database for a subset of materials is available, the same workflow can be applied to systematically explore the remaining chemical space. For novel materials, MLIP can first be used to reduce the search space by filtering for thermodynamic stability, while target properties are computed for a representative subset of compounds to train MLRMs for ML-HTP screening of the broader space. The workflow can also be applied iteratively, with results from DFT validations fed back into the ML models to improve their accuracy and predictive power, thereby generating new candidate materials and recovering promising compounds that may have been missed in earlier screening stages.

In the framework of this study, MLIP perform the critical task of structure optimization, which is traditionally handled by DFT-derived methods, while MLRMs predict the properties of the optimized structures, tasks that are typically carried out using DFT or DFT-derived methods. Together, MLIP and MLRMs enable a drop-in replacement for DFT in conventional HTP workflows. This replacement is general and can be readily extended to other properties, material classes, and DFT-based HTP pipelines, enabling accelerated HTP screening and discovery of new materials.

4 Methods

4.1 Composition and structure

This study screened two classes of Heusler compounds not included in HeuslerDB: (i) conventional quaternary Heuslers and (ii) all- d ternary and quaternary Heuslers. The ternary Heuslers were considered in regular, inverse, and half-Heusler structures [20]. For conventional quaternary compounds, we enumerated all combinations where X and Y are transition metals from the d -block (excluding Tc and Hg), and Z is a main-group element from groups 13, 14, or 15 of the p -block, as illustrated in Fig. 1(b).

In addition, La and Lu were included for X and Y because their $4f$ orbitals are either empty or fully filled. This exhaustive enumeration, accounting for symmetry constraints, yielded 131,544 unique compositions. For the all- d Heuslers, we extended the combinatorial space to include only d -block transition metals together with La and Lu across all four sites (X_1 , X_2 , Y , and Z), resulting in a separate set of 104,139 unique compositions.

4.2 ML-HTP workflow

The ML-HTP workflow, including the use of [MLIP](#) and [MLRM](#) together with the selection criteria, is schematically illustrated in Fig. 1(c) and described in detail below.

(a) Structure optimization

The initial lattice constant was estimated as the average value of known X_2YZ Heusler compounds in the [HeuslerDB](#) database that share two elemental species with the target composition. A conventional cell in cubic phase with this estimated lattice constant was then constructed. To generate initial structures, the lattice parameters of this cell were systematically varied: the a , b , and c were uniformly scaled by $\pm 10\%$ or $\pm 30\%$, and, alternatively, the c alone was scaled by $\pm 10\%$ or $\pm 30\%$. All generated structures were subsequently converted to the primitive unit cell and relaxed using the [eSEN-30M-OAM MLIP](#). The structure with the lowest energy after relaxation was identified as the ground state. The choice of [eSEN-30M-OAM](#) was motivated by its superior performance relative to other [MLIPs](#), as discussed in Sec. 2.3. The selection of initial structures was validated by a convergence test, which is provided in the Supplementary Materials.

(b) Thermodynamic stability from [MLIP](#) energies

For a compound to be thermodynamically stable against decomposition into its constituent elements or competing phases, the formation energy must be negative

($\Delta E < 0$) and the distance to the convex hull must be zero ($\Delta H = 0$). In practice, however, metastable phases ($\Delta H > 0$) at 0 K may become stabilized at finite temperature [36]. Following our previous work, we adopt a practical stability criterion of $\Delta E < 0.0$ eV/atom and $\Delta H < 0.22$ eV/atom, which has been shown to effectively capture experimentally accessible compounds [20]. Using the energies of ground state candidates, constituent elements and competing phases predicted by eSEN-30M-OAM, we computed ΔE and ΔH to assess thermodynamic stability.

(c) Property prediction using MLRMs

Using MLIP-optimized structures, the ω_{\min} , $\{\mathbf{m}_i\}$, T_c , and E_{aniso} were predicted with MLRMs trained on the HeuslerDB and additional computed data. The construction of these MLRMs is described in Sec. 2.5 and Sec. 2.6. Compounds were classified as dynamically stable for $\omega_{\min} > -10$ cm⁻¹, magnetic for $\sum_i |\mathbf{m}_i| > 0.1$ μ_B /f.u., magnetically stable for $T_c > 300$ K, and strong E_{aniso} candidates for $|E_{\text{aniso}}| > 1$ MJ/m³. Tetragonal compounds satisfying all of these conditions were designated as promising stable materials with strong E_{aniso} .

(d) DFT validation

The candidate list was validated with DFT calculations to assess the reliability of the ML-HTP workflow. Structure optimizations were performed starting from various initial spin configurations, consistent with our previous DFT-THP work. For conventional Heusler compounds, the magnetic moments at the X_1 , X_2 , and Y sites were initialized in configurations where they were either parallel or antiparallel to each other. For all- d Heuslers, spin arrangements on all four sites were considered. To capture possible high-spin and low-spin states, two initial magnitudes of the local moments ($|\mathbf{m}_i| = 1$ and 4 μ_B) were tested, along with a non-magnetic configuration ($|\mathbf{m}_i| = 0$). The MLIP-optimized structures served as the starting geometries. After structure relaxation, the ground state was identified by comparing total energies. For the resulting

ground states, we computed ΔE , ΔH , E_{aniso} , phonon, and T_c using VASP, OQMD, ALAMODE, and SPRKKR [37–42].

4.3 Computational methods

The MLIP-based structural optimizations were performed using the Atomic Simulation Environment (ASE) package [43]. The Fast Inertial Relaxation Engine (FIRE) optimizer was employed, with symmetry constraints enforced throughout the relaxation process [44]. To ensure consistency in reference energies for computing ΔE and ΔH , the elemental phases and competing phases were also optimized using the same MLIP. Their initial geometries were taken from DFT-optimized structures in the Open Quantum Materials Database (OQMD) database [37, 38].

The MLRMs were developed to predict ω_{min} , $\{\mathbf{m}_i\}$, T_c , and E_{aniso} . To leverage prior knowledge, we employed a frozen transfer learning strategy, as illustrated in Fig. 1(a). Each MLRM was initialized from the pretrained eSEN-30M-OAM MLIP, with the embedding layer and the first seven message-passing layers kept frozen, while the final three layers and the output layer were fine-tuned. This framework was implemented using a modified version of the FAIRChem package (v1) [45]. For the $\{\mathbf{m}_i\}$ MLRM training, the loss function was adapted to address the global sign ambiguity of magnetic moments, as described in Sec. 2.5. The training dataset consisted of HeuslerDB together with newly computed E_{aniso} and T_c values based on the optimized structures in HeuslerDB. The data were randomly partitioned into training, validation, and test sets in an 8:1:1 ratio. For $\{\mathbf{m}_i\}$, we used all ground-state entries, resulting in 27,864 data points. The ω_{min} data were available for all thermodynamically stable ground states, yielding 8,198 entries. For T_c , 2,106 data points were used, including 750 newly computed values. Since E_{aniso} data were not included in HeuslerDB, we calculated E_{aniso} for all magnetic tetragonal ground-state systems, obtaining 6,123 entries.

DFT calculations were performed primarily with [Vienna *ab initio* Simulation Package \(VASP\)](#) [46, 47], using the projector augmented wave (PAW) method and the generalized gradient approximation (GGA) with the Perdew–Burke–Ernzerhof (PBE) functional [48, 49]. ΔE , ΔH , phonon, and T_c were computed using OQMD, ALAM-ODE, and SPRKKR following the methodology of our previous DFT-HTP study of ternary Heusler compounds [20, 37–42]. Phonon calculations for the all-*d* compounds MnOsMnRe and MnReMnRu failed due to convergence issues in DFT, and these compounds were treated as unstable in the validation rate analysis. E_{aniso} was calculated as $E_{\text{aniso}} = E_{\perp} - E_{\parallel}$ using the force theorem [50–52]. Calculations were performed in the primitive cell with \mathbf{k} -meshes generated using [Python Materials Genomics \(pymatgen\)](#) at a density of 6000 \AA^{-3} , and the tetrahedron method with Blöchl corrections was applied [53, 54]. Input generation, structure manipulation, and symmetry analysis were carried out using [pymatgen](#), [ASE](#), ASE2SPRKKR, and spglib [38, 43, 53, 55, 56].

Data availability

The ML-HTP candidate list and DFT validation results are included in the Supplementary Materials. The complete set of all screened compounds, along with ML-predicted properties, will be made available through the [HeuslerDB](#) database at <https://www.nims.go.jp/group/spintheory/>.

Code availability

The underlying code for this study is not publicly available but may be made available to qualified researchers on reasonable request from the corresponding author.

Acknowledgments

This study was supported by MEXT Program: Data Creation and Utilization-Type Material Research and Development Project (Digital Transformation Initiative Center for Magnetic Materials) Grant Number JPMXP1122715503 and as “Program for Promoting Researches on the Supercomputer Fugaku” (Data-Driven Research Methods Development and Materials Innovation Led by Computational Materials Science, JPMXP1020230327). This study used computational resources of supercomputer Fugaku provided by the RIKEN Center for Computational Science (Project ID: hp240223), the computer resources provided by ISSP, U-Tokyo under the program of SCCMS, and the computer resources at NIMS Numerical Materials Simulator.

Author contributions

TT conceptualized, designed, and supervised the project; reviewed and edited the manuscript. TT and EX developed the methodology and code implementation; performed the calculations and analysis; EX drafted the manuscript.

Competing interests

All authors declare no financial or non-financial competing interests.

References

- [1] Sanvito, S. *et al.* Accelerated discovery of new magnets in the Heusler alloy family. *Science Advances* **3**, e1602241 (2017).
- [2] Zhang, H. High-throughput design of magnetic materials. *Electronic Structure* **3**, 033001 (2021).

- [3] Barwal, V. *et al.* Large magnetoresistance and high spin-transfer torque efficiency of $\text{Co}_2\text{Mn}_x\text{Fe}_{1-x}\text{Ge}$ ($0 \leq x \leq 1$) Heusler alloy thin films obtained by high-throughput compositional optimization using combinatorially sputtered composition-gradient film. *APL Materials* **12**, 111114 (2024).
- [4] Faleev, S. V. *et al.* Heusler compounds with perpendicular magnetic anisotropy and large tunneling magnetoresistance. *Physical Review Materials* **1**, 024402 (2017).
- [5] Hu, K. *et al.* High-throughput design of Co-based magnetic Heusler compounds. *Acta Materialia* **259**, 119255 (2023).
- [6] Hilgers, R., Wortmann, D. & Blügel, S. Machine Learning-based estimation and explainable artificial intelligence-supported interpretation of the critical temperature from magnetic ab initio Heusler alloys data. *Physical Review Materials* **9**, 044412 (2025).
- [7] Baigutlin, D. R., Sokolovskiy, V. V., Buchelnikov, V. D. & Taskaev, S. V. Machine learning algorithms for optimization of magnetocaloric effect in all-d-metal Heusler alloys. *Journal of Applied Physics* **136**, 183903 (2024).
- [8] Mitra, S., Ahmad, A., Biswas, S. & Kumar Das, A. A machine learning approach to predict the structural and magnetic properties of Heusler alloy families. *Computational Materials Science* **216**, 111836 (2023).
- [9] Xie, R., Crivello, J.-C. & Barreteau, C. Screening New Quaternary Semiconductor Heusler Compounds By Machine-Learning Methods. *Chemistry of Materials* **35**, 7615–7627 (2023).
- [10] Lu, Y., Sun, Y., Hou, C., Li, Z. & Ni, J. Explainable Attention CNN for Predicting Properties of Heusler Alloys. *The Journal of Physical Chemistry C* (2025).

- [11] Xie, T. & Grossman, J. C. Crystal Graph Convolutional Neural Networks for an Accurate and Interpretable Prediction of Material Properties. *Physical Review Letters* **120**, 145301 (2018).
- [12] Choudhary, K. & DeCost, B. Atomistic Line Graph Neural Network for improved materials property predictions. *npj Computational Materials* **7**, 1–8 (2021).
- [13] Barroso-Luque, L. *et al.* Open Materials 2024 (OMat24) Inorganic Materials Dataset and Models (2024). [arXiv:2410.12771](https://arxiv.org/abs/2410.12771).
- [14] Yamada, H. *et al.* Predicting Materials Properties with Little Data Using Shotgun Transfer Learning. *ACS Central Science* **5**, 1717–1730 (2019).
- [15] Lee, J. & Asahi, R. Transfer learning for materials informatics using crystal graph convolutional neural network. *Computational Materials Science* **190**, 110314 (2021).
- [16] Hoffmann, N., Schmidt, J., Botti, S. & Marques, M. A. L. Transfer learning on large datasets for the accurate prediction of material properties. *Digital Discovery* **2**, 1368–1379 (2023).
- [17] He, J., Rabe, K. M. & Wolverton, C. Computationally accelerated discovery of functional and structural Heusler materials. *MRS Bulletin* **47**, 559–572 (2022).
- [18] Noky, J., Zhang, Y., Gooth, J., Felser, C. & Sun, Y. Giant anomalous Hall and Nernst effect in magnetic cubic Heusler compounds. *npj Computational Materials* **6**, 1–8 (2020).
- [19] Xing, G., Masuda, K., Tadano, T. & Miura, Y. Chemical-substitution-driven giant anomalous Hall and Nernst effects in magnetic cubic Heusler compounds. *Acta Materialia* **270**, 119856 (2024).

- [20] Xiao, E. & Tadano, T. High-throughput computational screening of Heusler compounds with phonon considerations for enhanced material discovery. *Acta Materialia* **297**, 121312 (2025).
- [21] Fu, X. *et al.* Learning Smooth and Expressive Interatomic Potentials for Physical Property Prediction (2025). [arXiv:2502.12147](#).
- [22] Choudhary, K. *et al.* Unified graph neural network force-field for the periodic table: Solid state applications. *Digital Discovery* **2**, 346–355 (2023).
- [23] Deng, B. *et al.* CHGNet as a pretrained universal neural network potential for charge-informed atomistic modelling. *Nature Machine Intelligence* **5**, 1031–1041 (2023).
- [24] Kim, J. *et al.* Data-Efficient Multifidelity Training for High-Fidelity Machine Learning Interatomic Potentials. *Journal of the American Chemical Society* **147**, 1042–1054 (2025).
- [25] Yan, K. *et al.* A Materials Foundation Model via Hybrid Invariant-Equivariant Architectures (2025). [arXiv:2503.05771](#).
- [26] Yang, H. *et al.* MatterSim: A Deep Learning Atomistic Model Across Elements, Temperatures and Pressures (2024). [arXiv:2405.04967](#).
- [27] Hu, X. *et al.* Searching high spin polarization ferromagnet in Heusler alloy via machine learning. *Journal of Physics: Condensed Matter* **32**, 205901 (2020).
- [28] Miyazaki, H. *et al.* Machine learning based prediction of lattice thermal conductivity for half-Heusler compounds using atomic information. *Scientific Reports* **11**, 13410 (2021).

- [29] Kim, K. *et al.* Machine-learning-accelerated high-throughput materials screening: Discovery of novel quaternary Heusler compounds. *Physical Review Materials* **2**, 123801 (2018).
- [30] Liu, K. *et al.* Machine learning assisted development of Heusler alloys for high magnetic moment. *Computational Materials Science* **250**, 113692 (2025).
- [31] Hirohata, A. *et al.* Machine learning for the development of new materials for a magnetic tunnel junction. *npj Spintronics* **3**, 1–9 (2025).
- [32] Jain, A. *et al.* Commentary: The Materials Project: A materials genome approach to accelerating materials innovation. *APL Materials* **1**, 011002 (2013).
- [33] Schmidt, J. *et al.* Machine-Learning-Assisted Determination of the Global Zero-Temperature Phase Diagram of Materials. *Advanced Materials* **35**, 2210788 (2023).
- [34] Schmidt, J. *et al.* Improving machine-learning models in materials science through large datasets. *Materials Today Physics* **48**, 101560 (2024).
- [35] Kim, S. Y., Park, Y. J. & Li, J. Leveraging neural network interatomic potentials for a foundation model of chemistry (2025). [arXiv:2506.18497](https://arxiv.org/abs/2506.18497).
- [36] Sun, W. *et al.* The thermodynamic scale of inorganic crystalline metastability. *Science Advances* **2**, e1600225 (2016).
- [37] Saal, J. E., Kirklin, S., Aykol, M., Meredig, B. & Wolverton, C. Materials Design and Discovery with High-Throughput Density Functional Theory: The Open Quantum Materials Database (OQMD). *JOM* **65**, 1501–1509 (2013).
- [38] Bahn, S. & Jacobsen, K. An object-oriented scripting interface to a legacy electronic structure code. *Computing in Science & Engineering* **4**, 56–66 (2002).

- [39] Tadano, T. & Tsuneyuki, S. Self-consistent phonon calculations of lattice dynamical properties in cubic SrTiO₃ with first-principles anharmonic force constants. *Physical Review B* **92**, 054301 (2015).
- [40] Anharmonic force constants extracted from first-principles molecular dynamics: Applications to heat transfer simulations - IOPscience. <https://iopscience.iop.org/article/10.1088/0953-8984/26/22/225402>.
- [41] Ebert, H., Ködderitzsch, D. & Minár, J. Calculating condensed matter properties using the KKR-Green's function method—recent developments and applications. *Reports on Progress in Physics* **74**, 096501 (2011).
- [42] Liechtenstein, A. I., Katsnelson, M. I., Antropov, V. P. & Gubanov, V. A. Local spin density functional approach to the theory of exchange interactions in ferromagnetic metals and alloys. *Journal of Magnetism and Magnetic Materials* **67**, 65–74 (1987).
- [43] Hjorth Larsen, A. *et al.* The atomic simulation environment—a Python library for working with atoms. *Journal of Physics: Condensed Matter* **29**, 273002 (2017).
- [44] Bitzek, E., Koskinen, P., Gähler, F., Moseler, M. & Gumbusch, P. Structural Relaxation Made Simple. *Physical Review Letters* **97**, 170201 (2006).
- [45] Shuaibi, M. *et al.* FAIRChem (2025).
- [46] Kresse, G. & Furthmüller, J. Efficiency of ab-initio total energy calculations for metals and semiconductors using a plane-wave basis set. *Comput. Mater. Sci.* **6**, 15–50 (1996).
- [47] Kresse, G. & Furthmüller, J. Efficient iterative schemes for ab initio total-energy calculations using a plane-wave basis set. *Phys. Rev. B* **54**, 11169–11186 (1996).

- [48] Kresse, G. & Joubert, D. From ultrasoft pseudopotentials to the projector augmented-wave method. *Phys. Rev. B* **59**, 1758–1775 (1999).
- [49] Perdew, J. P., Burke, K. & Ernzerhof, M. Generalized Gradient Approximation Made Simple. *Phys. Rev. Lett.* **77**, 3865–3868 (1996).
- [50] Daalderop, G. H. O., Kelly, P. J. & Schuurmans, M. F. H. First-principles calculation of the magnetocrystalline anisotropy energy of iron, cobalt, and nickel. *Physical Review B* **41**, 11919–11937 (1990).
- [51] Xing, G., Miura, Y. & Tadano, T. Lattice dynamics and its effects on magnetocrystalline anisotropy energy of pristine and hole-doped YCo_5 from first principles. *Physical Review B* **105**, 104427 (2022).
- [52] Xing, G., Miura, Y. & Tadano, T. First-principles prediction of phase transition of YCo_5 from self-consistent phonon calculations. *Physical Review B* **108**, 014304 (2023).
- [53] Ong, S. P. *et al.* Python Materials Genomics (pymatgen): A robust, open-source python library for materials analysis. *Computational Materials Science* **68**, 314–319 (2013).
- [54] Blöchl, P. E., Jepsen, O. & Andersen, O. K. Improved tetrahedron method for Brillouin-zone integrations. *Physical Review B* **49**, 16223–16233 (1994).
- [55] ASE2SPRKKR software package — ASE2SPRKKR documentation. <https://ase2sprkkk.github.io/ase2sprkkk/>.
- [56] Togo, A., Shinohara, K. & Tanaka, I. Spglib: A software library for crystal symmetry search. *Science and Technology of Advanced Materials: Methods* **4**, 2384822

(2024).